# RESEARCH ARTICLE

**Key Points:**
- The ocean response to wind is amplified at near-inertial and low frequencies
- The ocean response is slightly anisotropic due to pressure gradients/friction
- The transfer function (frequency domain response) varies spatially/ seasonally

**Correspondence to:**
A. Fontán,
afontan@azti.es

# Anisotropic response of surface circulation to wind forcing, as inferred from high-frequency radar currents in the southeastern Bay of Biscay

**Almudena Fontán[1] and Bruce Cornuelle[2]**

[1]Marine Research Division, AZTI-Tecnalia, Pasaia, Spain, [2]Department of Climate, Atmospheric Science and Physical Oceanography, Scripps Institution of Oceanography, University of California, San Diego, California, USA

**Abstract** The short-term (less than 20 days) response of surface circulation to wind has been determined in waters of the southeastern Bay of Biscay, using wind impulse response (time domain) and transfer (frequency domain) functions relating high-frequency radar currents and reanalysis winds. The response of surface currents is amplified at the near-inertial frequency and the low-frequency and it varies spatially. The analysis indicates that the response of the ocean to the wind is slightly anisotropic, likely due to pressure gradients and friction induced by the bottom and coastline boundaries in this region. Thus, the transfer function at the near-inertial frequency decreases onshore due to the coastline inhibition of circularly polarized near-inertial motion. In contrast, the low-frequency transfer function is enhanced toward the coast as a result of the geostrophic balance between the cross-shore pressure gradient and the Coriolis forces. The transfer functions also vary with season. In summer, the current response to wind is expected to be stronger but shallower due to stratification; in winter, the larger mixed layer depth results in a weaker but deeper response. The results obtained are consistent with the theoretical description of wind-driven circulation and can be used to develop a statistical model with a broad range of applications including accurate oceanic forecasting and understanding of the coupled atmosphere-ocean influence on marine ecosystems.

## 1. Introduction

The Bay of Biscay is located in the intergyre zone of the North Atlantic, bounded by the North Atlantic Current and the Azores Current. Comparatively, the water circulation in the Bay of Biscay can be characterized as being relatively weak, especially, in the southeastern (SE) Bay of Biscay (Figure 1). However, currents here result from a complex combination of physical processes that occur simultaneously at a variety of spatial and temporal scales and amplitudes, e.g., a weak anticyclonic circulation in the abyssal plain, a poleward slope current, slope water oceanic eddies, tidal flows, wind-driven motions, density currents, and coastal upwelling and downwelling [*Koutsikopoulos and LeCann*, 1996]. In particular, the wind-driven currents are one of the major physical process governing the water circulation in both the open and the coastal ocean of the Bay of Biscay.

Within the Bay of Biscay, the research concerning the water circulation has been mainly focused on the poleward slope current and the associated slope water oceanic eddies [*Pingree and LeCann*, 1990, 1992; *García-Soto et al.*, 2002; *Gil*, 2003; *Le Cann and Serpette*, 2009; *Herbert et al.*, 2011; *Le Henaff et al.*, 2011; *Esnaola et al.*, 2013, among others], leaving, to some extent, the water circulation response to the wind action in the background. In particular, the research undertaken on wind-induced currents in the SE Bay of Biscay is scarce and regularly based on model simulation or short-term time series and fixed locations [*Ibáñez*, 1979; *Álvarez Salgado et al.*, 2006; *González et al.*, 2004; *Fontán et al.*, 2009, 2013a]. In the meantime, large spatial coverage high-frequency (HF) radar measurements have been undertaken in the SE Bay of Biscay. The research on those measurements by *Rubio et al.* [2011] described the spatial and temporal variability of the near-inertial currents in waters of the SE Bay of Biscay. Based on those HF radar currents, *Fontán et al.* [2013b] determined the simultaneous wind-current interaction spatial patterns and time scales in the same region at low-frequencies, without having to consider the past wind conditions. More recently, *Solabarrieta et al.* [2014] described seasonal, near-inertial, and tidal variability of surface circulation based on the same HF radar observations.
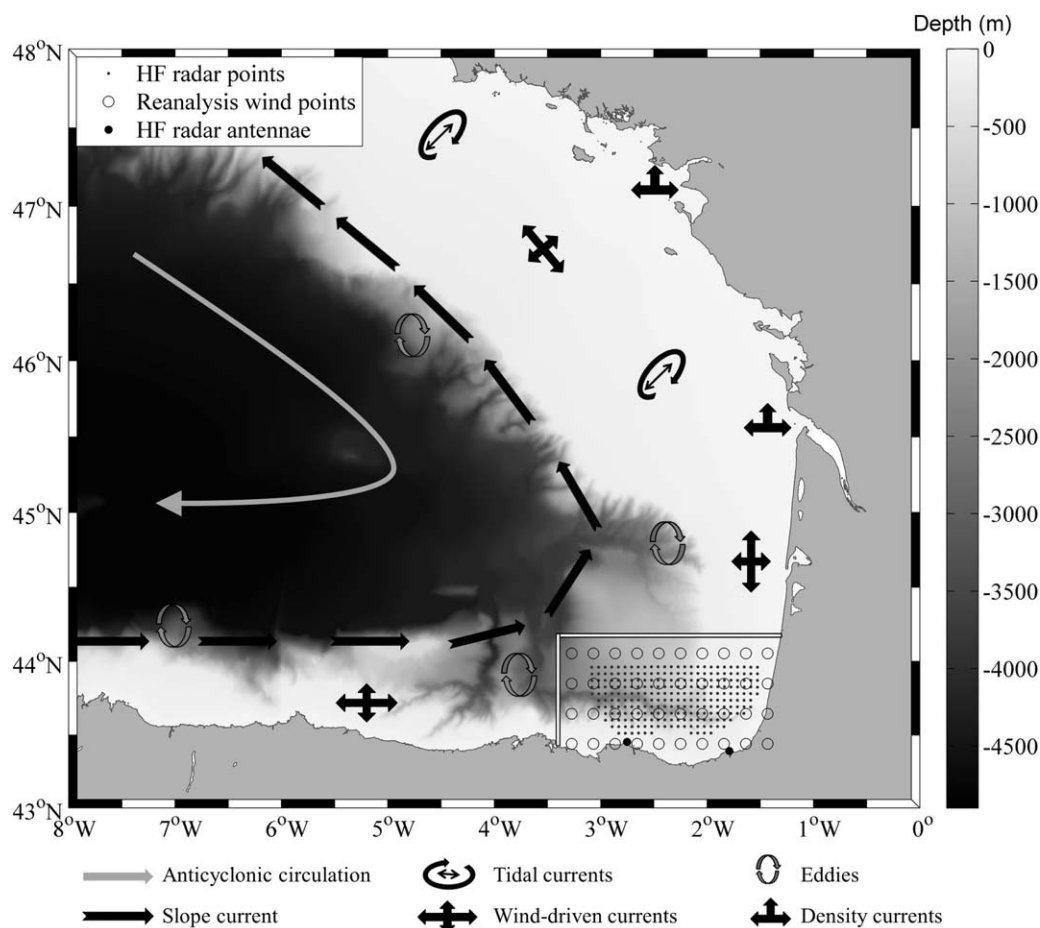
**Figure 1.** The location of the HF radar points with more than 90% data coverage, the HF radar stations and the reanalysis wind grid points are indicated by a rectangle. An approximate schematic illustration of the main currents in the region is also provided (the reader is referred to *Ferrer et al.* [2009], for a more detailed illustration).

As above mentioned, the circulation is driven primarily by the wind forcing in the open and the coastal ocean regions of the Bay. It should be underlined, however, that the wind-current interaction spatial patterns and time scales vary spatially from coastal to open sea regions. Therefore, a complex overall pattern of air-sea interactions, strongly modified by a number of factors, is established. For instance, the complex coastline (i.e., change of orientation) and bottom topography (i.e., fractured by submarine canyons as shown in Figure 1) induce horizontal pressure gradients and friction. These result in an anisotropic response of coastal currents to the wind action, namely, the response can depend upon the wind direction. In general, the current response to wind action has been assumed to be isotropic, meaning that the response of the current relative to wind direction does not depend on wind direction [*Ekman*, 1905; *Gonella*, 1972; *Río and Hernández*, 2003]. This simplifies the theory, and is a good approximation away from boundaries or strong vorticity gradients. Near the coast, *Ng* [1993] found anisotropic coupling between low-passed wind and current observations. Recently, *Kim et al.* [2009] derived a statistical coastal wind response model that supports anisotropic and asymmetric surface current response to wind action. These investigators obtained a comprehensive representation of the relationship between the wind and currents from diurnal to upwelling time scales, by estimating the transfer function. This function can be inversely Fourier transformed into the time domain, to obtain the wind impulse response function. *Elipot and Gille* [2009] derived transfer functions for nine idealized models in order to study the frequency response of the ocean to wind stress forcing. *Kim et al.* [2010] determined the spatial and seasonal variation of the transfer function in waters off San Diego. The authors concluded that the transfer function at the near-inertial frequency decreases toward the coastline, whereas it increases near the coast at low-frequencies due to coastline boundaries. *Kim and Kosro* [2013] have reported decorrelation time and length scales of near-inertial clockwise motions in coastal

waters off Oregon. More recently, *Kim and Crawford* [2014] have described resonant currents driven by winds near the critical latitude (i.e., 30°N/S where inertial-diurnal resonance occurs) using transfer functions.

The present investigation aims to apply statistical modeling, previously used offshore San Diego [*Kim et al.*, 2009, 2010] (wind impulse response and transfer functions) to investigate the surface current response to wind in the SE Bay of Biscay. In addition, this study attempts to extend the results obtained by *Fontán et al.* [2013b] by considering not only the influence of simultaneous winds on surface currents, but also the effect of the past wind conditions. Furthermore, the study focuses on the response of surface currents to wind in order to complement the results obtained by *Fontán et al.* [2013b] dealing only with low-frequency wind-induced currents. In particular, the main aims are to: (a) investigate the response of the ocean to the wind forcing on time scales of hours to 20 days, (b) examine the isotropic and anisotropic wind impulse response functions, and (c) determine spatial and seasonal variability in the transfer functions. This paper is organized as follows: section 2 describes the observations used in this investigation. Section 3 deals with the description of the weighted and tapered least squares methodology. In section 4, the spatial patterns and the spectral characteristics of surface currents and winds are given. Section 5 deals with the isotropic and anisotropic wind impulse response functions and the spatial variability of the transfer function. The seasonal variability of the transfer function at the low-frequency and the near-inertial frequency is explored in section 6. Finally, the main conclusions are summarized in section 7.

## 2. Observations

The response of surface circulation to wind forcing has been estimated using hourly HF radar currents and reanalysis winds for 2 years (2011–2012). In 2009, the Directorate of Emergency Attention and Meteorology (Basque Government) upgraded the operational data acquisition system, consisting of coastal stations and deep-sea buoys, with the installation of two HF radar stations in the coast of the SE Bay of Biscay (Figure 1). The HF (4.5 MHz) radar system has been operational since 2009 and it covers a roughly 150 km range with 5 km radial resolution. The data were preprocessed by applying the standard procedures in agreement with the manufacturer's recommendations. Thus, the radial velocities were obtained using the multiple signal classification (MUSIC) algorithm [*Schmidt*, 1986]. Afterward, the radial velocities were 3 h moving averaged to increase the statistical robustness of the estimates. Whenever the angle between two radials was less than 30°, the data were disregarded. A least squares approach was applied to radial data to obtain total velocities with an interpolation radius of 20 km. Subsequently, the resulting data were tested for spikes, stationary data, and out of range values. Finally, hourly currents were derived over a regular grid with spatial resolution of 5 km $\times$ 5 km. In this study, the HF radar points with at least 90% of data availability were selected for subsequent analysis (Figure 1).

Because we wish to explore the response of the ocean to the wind, the main semidiurnal tidal constituents ($M_2$, $S_2$, $N_2$, and $K_2$) were removed from the total currents by least squares fitting. The diurnal tidal constituents were not eliminated as the diurnal tidal currents are very weak in the SE Bay of Biscay [*Le Cann*, 1990]. Furthermore, the diurnal tidal currents are much weaker than the currents induced by the land-sea breezes, i.e., nontidal [*Fontán et al.*, 2013a].

The hourly wind components at 10 m above sea level (a.s.l.) of the Climate Forecast System Version 2 (CFSV2) for the period 2011–2012, provided by the National Centers for Environmental Prediction (NCEP), have been used in this study [*Saha et al.*, 2010, 2014]. The data from CFSV2 can be considered identical to CFSR (Climate Forecast System Reanalysis), except for the spatial resolution which increases from approximately 0.3° to 0.2°. *Fontán* [2013] validated the reanalysis winds (CFSR), for the period 2002–2010, by comparison with the wind observations from deep-sea buoys in the region. The reanalysis winds show good agreement with the observational data, with correlation coefficients of 0.86 $\pm$ 0.10, root-mean-square differences of 1.21 $\pm$ 0.09 m s$^{-1}$ and mean absolute errors of 0.44 $\pm$ 0.05 m s$^{-1}$. The meridional winds show lower correlation coefficients than the zonal winds; this could be related to the influence of the coastal boundaries. Also, the CFSV2 winds for the period 2011–2012 have been compared with observational winds with similar results. Likewise, *Álvarez et al.* [2014] compared CFSR winds and buoy wind data in the same region, concluding that CFSR winds are consistent with the observations.

## 3. Methods

The wind impulse response function describes the response of the water circulation to the wind forcing in the time domain. In the frequency domain, the response function is known as the transfer function, which

is defined as the ratio of the complex Fourier coefficients of the current to those of the wind at each frequency. In general, the response of the currents to the wind action has been estimated by the transfer function in the frequency domain [*Weller*, 1981; *Simons*, 1984; *Elipot*, 2006; *Elipot and Gille*, 2009; *Kim et al.*, 2009, 2010, among others]. The time domain equivalent has been less extensively used for this purpose. However, within this contribution, we have preferred to determine the response function in the time domain by least squares fitting, since the HF radar currents contain data gaps (less than 10%), which make spectral methods difficult. The presence of missing values in the HF radar currents was handled selecting only those time steps with full spatial data coverage. Once the response function has been determined in the time domain, it can be easily Fourier transformed to obtain the transfer function in the frequency domain, because it does not contain any missing values.

The wind impulse response function in the time domain ($\vec{g}(\tau)$) relating the horizontal surface current ($\vec{u}(t)$) at a single $(x, y)$ point at all observed times, to the 10 m wind forcing at time $\tau$ before the present, is defined as:

$$\vec{u}(t) = \sum_{k=0}^{M} \vec{g}(k\Delta t)\vec{w}(t - k\Delta t) + \vec{r}(t) \tag{1}$$

where $\vec{w}(t - k\Delta t)$ is the $k$ hours time-lagged horizontal vector wind, $\vec{r}(t)$ is the vector misfit at each observed time, $\Delta t = 1$ h is the time step, $\tau = M\Delta t$ is the maximum time lag considered, and $M = 481$.

This is a simplification of the Green's function for current response to wind, which includes winds at all forcing points. In this study, we use wind at the nearest reanalysis grid point, but similar results were found using wind averaged within radii up to 150 km. We also assume that the system is stationary, so that the impulse response depends only on time lag, except for one case where summer and winter are considered separately.

The equation (1) can be rewritten in matrix form by using column vectors to represent the time dependent values, so that **u** and **v** are the zonal and meridional surface currents, respectively. Likewise, $\mathbf{W}_x$ and $\mathbf{W}_y$ are the time-lagged wind matrices for zonal and meridional wind, respectively. For example, the matrix forms of **u** and $\mathbf{W}_x$ are:

$$\mathbf{u} = \begin{bmatrix} u(t_0) \\ u(t_0 + \Delta t) \\ \vdots \\ u(t_0 + (N-1)\Delta t) \end{bmatrix} \tag{2}$$

$$\mathbf{W}_x = \begin{bmatrix} w_x(t_0) & w_x(t_0 - \Delta t) & \cdots & w_x(t_0 - M\Delta t) \\ w_x(t_0 + \Delta t) & w_x(t_0) & \cdots & w_x(t_0 - (M-1)\Delta t) \\ \vdots & \vdots & \ddots & \vdots \\ w_x(t_0 + (N-1)\Delta t) & w_x(t_0 + (N-2)\Delta t) & \cdots & w_x(t_0 + (N-M)\Delta t) \end{bmatrix} \tag{3}$$

where $t_0$ is the starting time of the $N$ observations.

The impulse responses of zonal and meridional current to zonal and meridional wind, or the parallel responses, as a function of time lag are denoted as column vectors $\mathbf{g}_{ux}$ and $\mathbf{g}_{vy}$, respectively, and the responses of meridional and zonal current to zonal and meridional wind, or the perpendicular responses, as column vectors $\mathbf{g}_{vx}$ and $\mathbf{g}_{uy}$, respectively. For example,

$$\mathbf{g}_{ux} = \begin{bmatrix} g_{ux}(0) \\ g_{ux}(\Delta t) \\ \vdots \\ g_{ux}(M\Delta t) \end{bmatrix} \tag{4}$$

The combined equations for the wind-driven surface current are:

$$
\begin{bmatrix} \mathbf{u} \\ \mathbf{v} \end{bmatrix} = \begin{bmatrix} \mathbf{W}_x & \mathbf{W}_y & 0 & 0 \\ 0 & 0 & \mathbf{W}_x & \mathbf{W}_y \end{bmatrix} \begin{bmatrix} \mathbf{g}_{ux} \\ \mathbf{g}_{uy} \\ \mathbf{g}_{vx} \\ \mathbf{g}_{vy} \end{bmatrix} + \begin{bmatrix} \mathbf{r}_u \\ \mathbf{r}_y \end{bmatrix}
\tag{5}
$$

$\mathbf{r_u}$ and $\mathbf{r_v}$ are column vectors of residuals (misfits or "noise") in the relations for zonal and meridional surface current, respectively, at the observation times.

If the system is isotropic, then $\mathbf{g}_{ux} = \mathbf{g}_{vy}$, and $\mathbf{g}_{uy} = -\mathbf{g}_{vx}$, for parallel and perpendicular responses, respectively. However, if the residuals and the impulse response functions are not expected to be correlated between $\mathbf{u}$ and $\mathbf{v}$, then the problems for $\mathbf{u}$ and $\mathbf{v}$ can be solved separately and the wind impulse response function can be estimated by minimizing the sum of the squared residuals in (1) or (5) in a least squares sense. If the residuals are expected to be of uniform size and vanishingly small with respect to the expected signal, the estimation simplifies to "ordinary least squares" (OLS) estimates for $\mathbf{g_u}$ or $\mathbf{g_v}$. For example, the impulse response for $\mathbf{u}$ is estimated as:

$$
\widetilde{\mathbf{g_u}}_{OLS} = \left( \mathbf{W}^T \mathbf{W} \right)^{-1} \mathbf{W}^T \mathbf{u}
\tag{6}
$$

where $\widetilde{\mathbf{g_u}}_{OLS}$ is the ordinary least squares estimated impulse response function and $\mathbf{W} = [\mathbf{W}_x \, \mathbf{W}_y]$ is the time-lagged vector wind.

In the current study, a weighted and tapered least squares solution [*Wunsch*, 1996] was applied to account for finite Signal-to-Noise Ratios (SNR) and to build in prior expectations that the response to wind decays with time. This means that recent wind conditions have the most influence. The tapered least squares method uses quantified expectations for the sizes of the response functions and the residuals to trade the magnitude of the estimated impulse response function against that of the residuals. Assuming Gaussian statistics, the prior expectations are quantified by covariance matrices of uncertainty for the residuals ($\mathbf{R}$) and for the parameters ($\mathbf{P}$) of the ordinary least squares. For simplicity, $\mathbf{R}$ has been assumed to be a scalar times the identity matrix, meaning that the misfits are assumed to be uncorrelated and with identical probability distributions. The prior uncertainty for the model parameters, $\mathbf{P}$, has also been assumed to be diagonal if no isotropy is expected ($\mathbf{u}$ and $\mathbf{v}$ response independent), with variance decaying with lag. In this particular case, the estimated impulse response function ($\tilde{\mathbf{g}}_u$) for $\mathbf{u}$ can be determined by:

$$
\widetilde{\mathbf{g}}_u = \left( \mathbf{W}^T \mathbf{R}^{-1} \mathbf{W} + \mathbf{P}^{-1} \right)^{-1} \mathbf{W}^T \mathbf{R}^{-1} \mathbf{u}
\tag{7}
$$

The use of the signal and noise covariances results in a regularized regression estimate [*Kim et al.*, 2009] which is biased toward zero, so that the estimate goes to zero at low SNR. This regularization was adjusted so that the cross-validation skill of the regression on independent data was similar to the skill on the training data used to estimate the coefficients. If the regularization is too small, the skill on the training data can greatly exceed that on the independent data, a problem known as "artificial predictability." Once the regularization was set, the regression was redone on the entire data set, but the results were similar to those found for subsets used in the cross-validation tests.

For comparison with Ekman theory, the estimated wind impulse response function has been Fourier transformed to the transfer function in the frequency domain. The transfer function ($\mathbf{G}$) is defined as the ratio of the complex Fourier coefficients of the current to those of the wind at each discrete frequency $\omega_j$ as follows:

$$
\mathbf{G}(\omega_j) = \frac{\mathbf{U}(\omega_j)}{\mathbf{T}(\omega_j)}
\tag{8}
$$

where $\mathbf{U}$ and $\mathbf{T}$ are the Fourier transforms of $\mathbf{u}$ and $\mathbf{w}$, respectively. $\mathbf{G}$ is complex valued at any frequency $\omega_j$.

In this study, the transfer functions have been computed using rotary spectral analysis. The rotary spectral analysis allows us to decompose vector data sets into circularly polarized clockwise (at negative

frequencies) and anticlockwise (at positive frequencies) components at each frequency [*Gonella*, 1972]. To this end, the response function components are written in complex notation as follows:

$$\mathbf{g}_x(\tau) = \mathbf{g}_{ux}(\tau) + i\mathbf{g}_{vx}(\tau)$$
$$\mathbf{g}_y(\tau) = \mathbf{g}_{uy}(\tau) + i\mathbf{g}_{vy}(\tau)$$

(9)

where $i = \sqrt{-1}$, and $\mathbf{g}_x$ and $\mathbf{g}_y$ are the response functions for the zonal and meridional time-lagged winds, respectively.

For instance, the Fourier transform of the complex time series $\mathbf{g}_x(\tau)$ at each frequency is denoted by:

$$\mathbf{G}_x(\omega_j) = \frac{1}{\tau} \int_0^\tau \mathbf{g}_x(\tau) e^{-i\omega_j \tau} \, d\tau = |\mathbf{G}_x(\omega_j)| e^{i\theta\omega_j}$$

(10)

where $|\mathbf{G}_x|$ is the amplitude or the absolute value of the transfer function and $\theta$ is the phase defined as:

$$\theta(\omega_j) = arctan\left(\frac{Im(\mathbf{G}_x(\omega_j))}{Re(\mathbf{G}_x(\omega_j))}\right)$$

(11)

On the other hand, the separate spectral analysis of currents and winds was also obtained using rotary spectral analysis, but in this case, the Blackman-Tukey method was used to determine the Power Spectral Density (PSD). For this purpose, the autocovariance function of currents and winds was determined with maximum time lag of 20 days. Then, the observed autocovariance functions were Fourier transformed to the frequency domain to obtain the PSD. It is worth noting that the HF radar currents contain data gaps (less than 10% of missing data). Up to 96% of the data gaps extend from a few hours to 1 day, with the remainder of the gaps extending from 1 to 2 days, and occurring simultaneously at all locations. As such, we filled the missing values with zeros to perform spectral analysis since it is difficult to interpolate long data gaps that occur simultaneously at all the points. The comparison of the spectra performed on a time series with no gaps and on two time series, with the gaps (distributed as in the HF radar data set) interpolated and filled with zeros, shows that there is not difference between the spectral analyses (not shown). Finally, the spectral estimates were smoothed by a Hanning window to decrease sidelobes.

## 4. Spatial Patterns and Spectral Characteristics of Surface Currents and Winds

To examine the spatial patterns of surface winds and currents, the variance ellipses or principal axes have been determined as shown in Figure 2. The major principal axes for the total winds are oriented in the east-west direction for most of the locations as expected, since the westerlies are the prevailing winds in the midlatitudes. The locations close to the coast (mainly in the southern-most part of the domain) rotate to the northwest-southeast direction. This is in agreement with *Usabiaga et al.* [2004], who concluded that the southerlies are more frequent in winter and autumn, whereas the northerlies prevail in spring and summer. The major principal axes for the detided currents show that the ellipses are elongated with a north-southerly, northeast-southwesterly or east-westerly direction depending on the location.

In order to explore the spectral characteristics of surface winds and detided surface currents, the joint Probability Density Distribution (PDF) of PSD and frequency, for all points in the domain, has been determined (Figure 3). The joint PDF expresses the probability of occurrence associated with each possible pair of values of PSD and frequency.

The spectrum for the winds (Figure 3a) peaks at low-frequency and at the diurnal period for both clockwise and anticlockwise motions. The diurnal peaks are associated with the diurnal wind resulting from land-sea breezes. In general, there is no preference for either clockwise or counterclockwise rotation of the diurnal winds in the individual spectra (not shown). The diurnal energy increases toward the coast (not shown), which is consistent with the fact that the strength of the land-sea breezes increases onshore. For the detided surface currents (Figure 3b), the dominant peaks are related to the near-inertial currents as noted by *Rubio et al.* [2011]. The spectrum shows a dominance of clockwise over anticlockwise motions as the near-inertial currents rotate clockwise in the northern hemisphere. The presence of a weaker anticlockwise energy has also been reported by *Kim and Kosro* [2013], who concluded that this implies elliptical motions of near-inertial currents rather than pure circular motions. Also, well-defined but minor clockwise diurnal
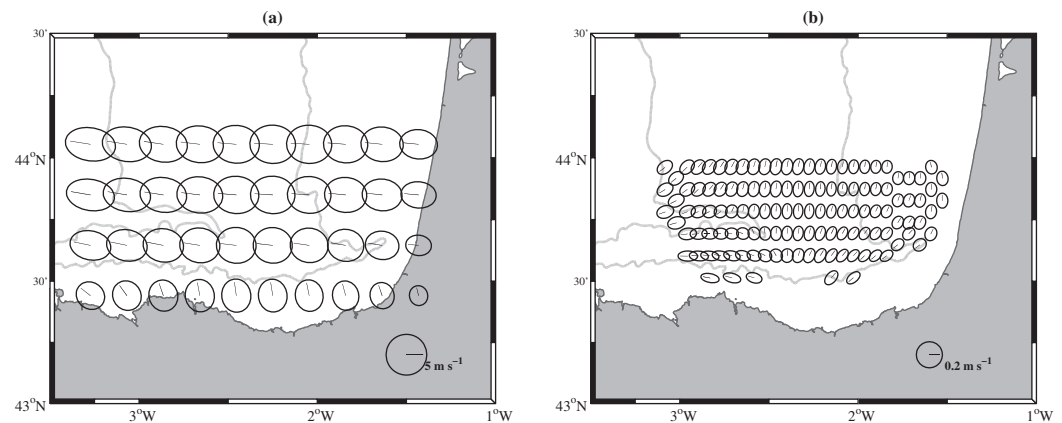
**Figure 2.** The variance ellipses together with the major axes for: (a) surface reanalysis winds and (b) HF radar detided surface currents. Note: one every two HF radar points are shown. Bathymetric contours show the 200 and 2000 m isobaths.

peaks associated with the influence of the breezes on surface currents can be observed in Figure 3b. The energy related to anticlockwise diurnal currents is much smaller, because it is far from the clockwise inertial resonance.

## 5. Isotropic and Anisotropic Response of Surface Currents to Wind Forcing

This section aims to investigate the short-term response of the ocean to the wind forcing and to determine whether the current response to wind is isotropic or anisotropic in the SE Bay of Biscay. In order to achieve this objective with gappy observations, the isotropic and anisotropic wind impulse response functions were calculated in the time domain. Afterward, both isotropic and anisotropic response functions were Fourier transformed to the frequency domain to obtain the transfer functions. The transfer functions for the isotropic and anisotropic approaches are shown in Figures 4 and 5, respectively.

For the isotropic approach, the PDFs of the amplitude and the phase of the transfer function in the frequency domain are shown in Figures 4a and 4b. The transfer function is only shown for the zonal wind because isotropy means that the response (relative to wind direction) is the same for wind from any direction. Note that the phase is most uncertain where the amplitude of the driving or the response function is small. The PDF peaks at the near-inertial frequency and the low-frequency (Figure 4a). The phase is nearly zero for both near-inertial and the low-frequency responses and it varies between $-45°$ and $45°$ as expected (Figure 4b). The resonance at the near-inertial frequency is consistent with the Ekman theory of surface currents [*Ekman*, 1905] and it is in agreement with the results of other authors [*Gonella*, 1972; *Río*
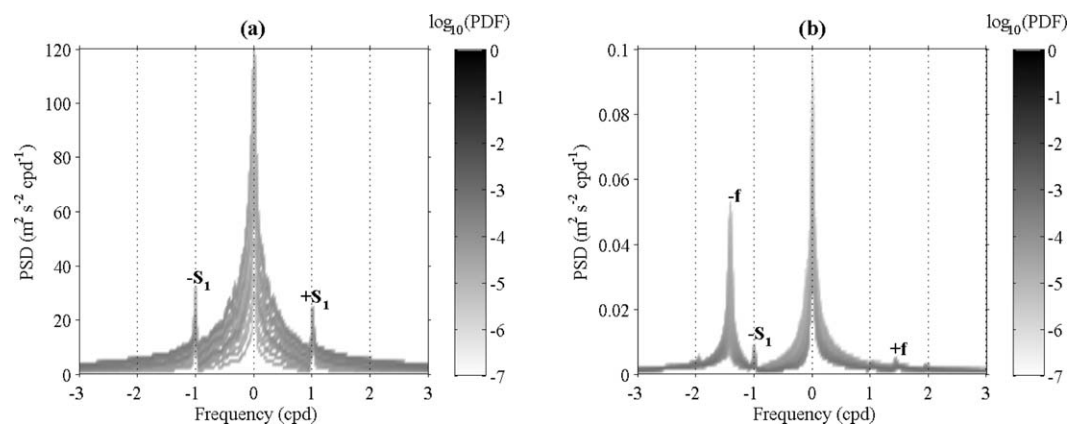


**Figure 3.** The joint Probability Density Function (PDF) of smoothed Power Spectral Density (PSD), with 70 degrees of freedom, and frequency for all the points of: (a) surface reanalysis winds and (b) HF radar detided surface currents. Note: $\omega = \pm S_1$ indicates the clockwise/counterclockwise diurnal frequency and $\omega = \pm f$ the clockwise/counterclockwise near-inertial frequency.
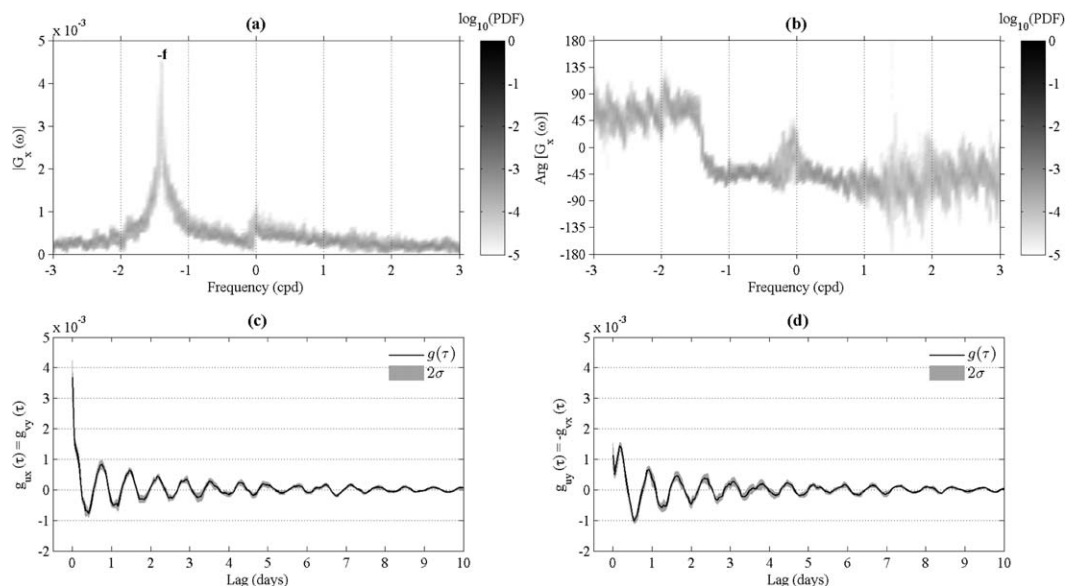
**Figure 4.** The joint Probability Density Function (PDF) of (a) the amplitude and (b) the phase of the isotropic transfer functions together with the temporal evolution of the isotropic (c) parallel and (d) perpendicular impulse response functions. Note: the average ± standard deviation of the impulse response functions is shown. $\omega = -f$ indicates the clockwise near-inertial frequency.

*and Hernández*, 2003; *Kim et al.*, 2009]. The temporal evolution of the response functions shows clockwise near-inertial variability (Figures 4c and 4d); these functions decay to small values by 7 days, although some response can be seen out to 10 days. This is also in agreement with the results of *Kim et al.* [2009] and *Kim and Kosro* [2013], who concluded that the decorrelation time scales of the near-inertial motions vary in between 2 and 6 days from coastal to open ocean, respectively.

For the anisotropic model, the PDF of the transfer function is shown in Figure 5. The anisotropic function consists of four independent terms: the response of the zonal current to zonal and meridional wind, $\mathbf{g}_{ux}$ and $\mathbf{g}_{uy}$, respectively, and the response of the meridional current to zonal and meridional wind, $\mathbf{g}_{vx}$ and $\mathbf{g}_{vy}$, respectively. As mentioned above, the rotary spectra have been determined by means of: $\mathbf{g}_x = \mathbf{g}_{ux} + i\mathbf{g}_{vx}$ and $\mathbf{g}_y = \mathbf{g}_{uy} + i\mathbf{g}_{vy}$. The PDFs of the magnitude of anisotropic transfer function (Figures 5a and 5c) show peaks at the clockwise near-inertial frequency and at the low-frequency as expected. The PDFs also show the presence of minor anticlockwise near-inertial frequency in agreement with the spectral characteristics of surface currents in Figure 3b. The PDFs of the magnitude of the transfer functions for the zonal and meridional winds are not equal, indicating that the response of the ocean to the wind is somewhat anisotropic. The temporal evolution of the response functions in Figures 5e and 5f also confirms that the response function is slightly anisotropic. Again, the response functions show near-inertial variability which decays to zero after approximately 7 days.

It is worth clarifying that the wind intensity decreases toward the coast as shown in Figure 2. This would lead to a decrease of the SNR for the inertial wind response per unit forcing near the coast, where the wind forcing decreases. However, we believe that the decrease is not caused by low SNR, and that the uncertainty in the near-inertial transfer function estimate near the coast is small. The variation in the phase of the transfer function at the near-inertial frequency across the domain (Figures 4b, 5b, and 5d) is small, and the phase is a sensitive indicator of error. For example, the phase is scattered at frequencies higher than ±2 cpd. At these high-frequencies, both the driving wind energy and the response are small, and the estimates are uncertain, in contrast to the estimates at the near-inertial frequency, which are not. In addition, it can be seen in Figure 3a, that at low-frequencies, there is almost no place in the domain with wind energy as small as above ±2 cpd, showing that SNR is likely not a problem in estimating the low-frequency response. Again, there is small phase variability at low-frequency (Figures 4b, 5b, and 5d), also indicating the robustness of the estimated transfer functions.

It should be emphasized that the HF radar measures ocean currents at various spatial and temporal scales such as tidal currents, density-driven, and currents driven by wind forcing. In the SE Bay of Biscay, the tidal
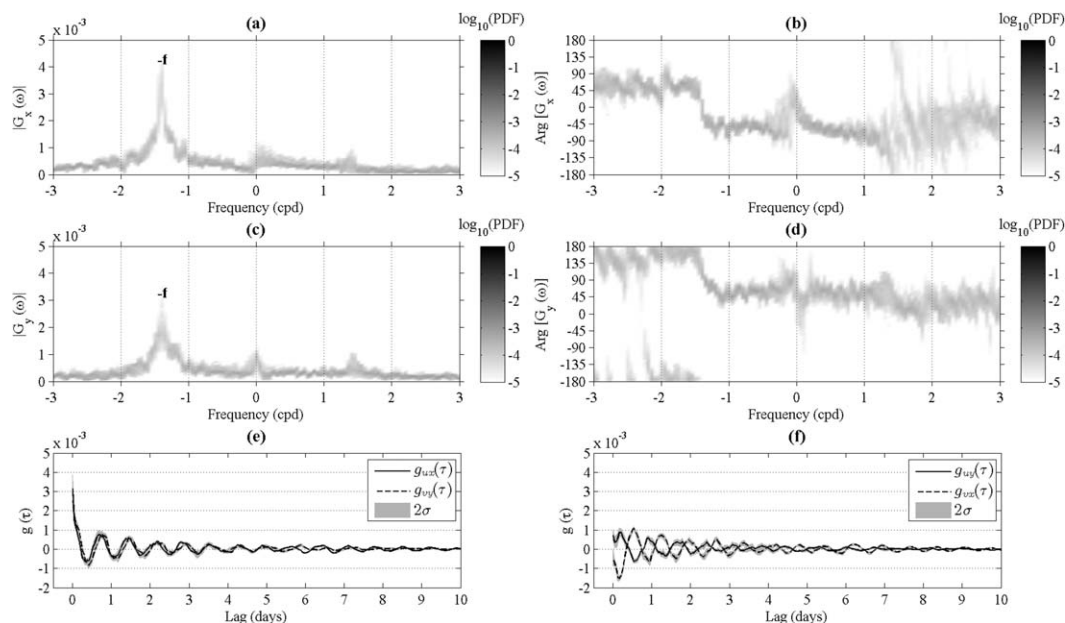
**Figure 5.** The joint Probability Density Function (PDF) of (a and c) the amplitude and (b and d) the phase of the anisotropic transfer functions together with the temporal evolution of the anisotropic (e) parallel and (f) perpendicular impulse response functions. Note: the average $\pm$ standard deviation of the impulse response functions is shown. $\omega = -$f indicates the clockwise near-inertial frequency.

currents (to the south of 45°N) are very weak, due to the narrowness of the continental shelf [*Koutsikopoulos and LeCann*, 1996]. The density-driven flow is small, due to the low river runoff in the region. In the particular case of surface currents driven by wind, these can be classified into wind-driven currents accelerated by wind forcing and wave-drift currents (Stokes drift) induced by nonlinearity of surface waves. The estimation of the Stokes drift velocity, from a deep water buoy in the region, is about $7 \pm 7$ cm s$^{-1}$ for the period 2011–2012. It is worth mentioning that the Stokes drift could contribute to the estimated response function in the low-frequency range [*Ardhuin et al.*, 2009, Figure 3a], where it can be as strong as the Ekman response. In the data set considered here, the estimated Stokes drift is weakly correlated with the HF radar observations (correlation coefficients around 0.2). Consequently, in the frequency range we consider, the surface water circulation can be said to be mainly controlled by the local direct wind forcing.

On average, the isotropic model explains approx. $39 \pm 12\%$ and $36 \pm 10\%$ of variance for the zonal and meridional currents, respectively. The largest values are obtained for the anisotropic model, which explains around $45 \pm 13\%$ and $42 \pm 9\%$ of variance for the zonal and meridional currents, respectively. This indicates that the response of the surface circulation to wind forcing is weakly anisotropic in the SE Bay of Biscay. The anisotropy is enhanced nearshore, where the fraction of variance explained by the anisotropic model is around 8–16% higher than that explained by the isotropic model. In contrast, offshore, the anisotropic model explains only 2–4% more variance than the isotropic model. This is consistent with the expectation that the coast is the source of the anisotropy. It is worth noting that these variance values may be highly dependent on the quality of the wind fields used, i.e., smoothed reanalysis winds versus real wind observations.

On the other hand, the estimated speed factors, the ratio of the wind-driven surface current speed to the wind speed vary considerably in the literature: from 1% to 11% [*Ekman*, 1905; *Kim et al.*, 2009; *Yoshikawa and Masuda*, 2009; *Kim et al.*, 2010, among others]. However, most of the authors do not specify the depth at which the wind factor should be applied or the height of the wind observations. Here, the average speed factors are $1.1 \pm 0.2\%$, which are in the lower band of the estimated values in the literature. This may be related to the fact that the factor is derived from smoothed reanalysis winds at 10 m a.s.l. and also from HF radar currents of the upper 2–3 m of the water column.

As mentioned above, the response of the currents to the wind forcing contains peaks at the near-inertial frequency and at the low-frequency. The spatial distribution of the magnitude of the anisotropic transfer function at the clockwise near-inertial frequency and at the low-frequency can be observed in Figure 6. The
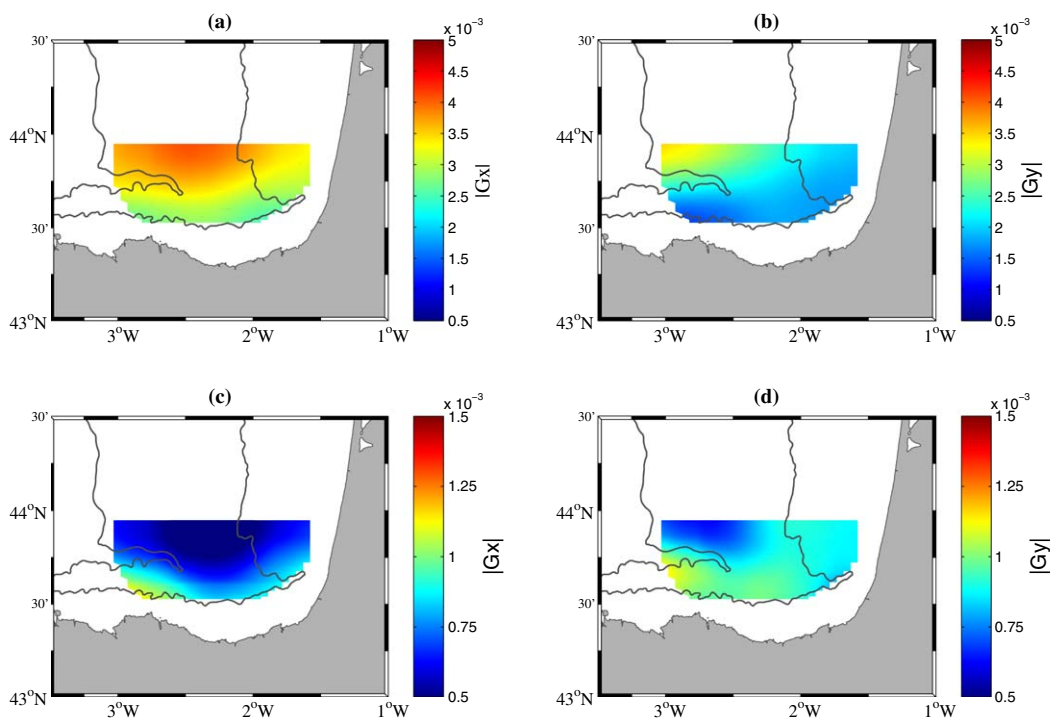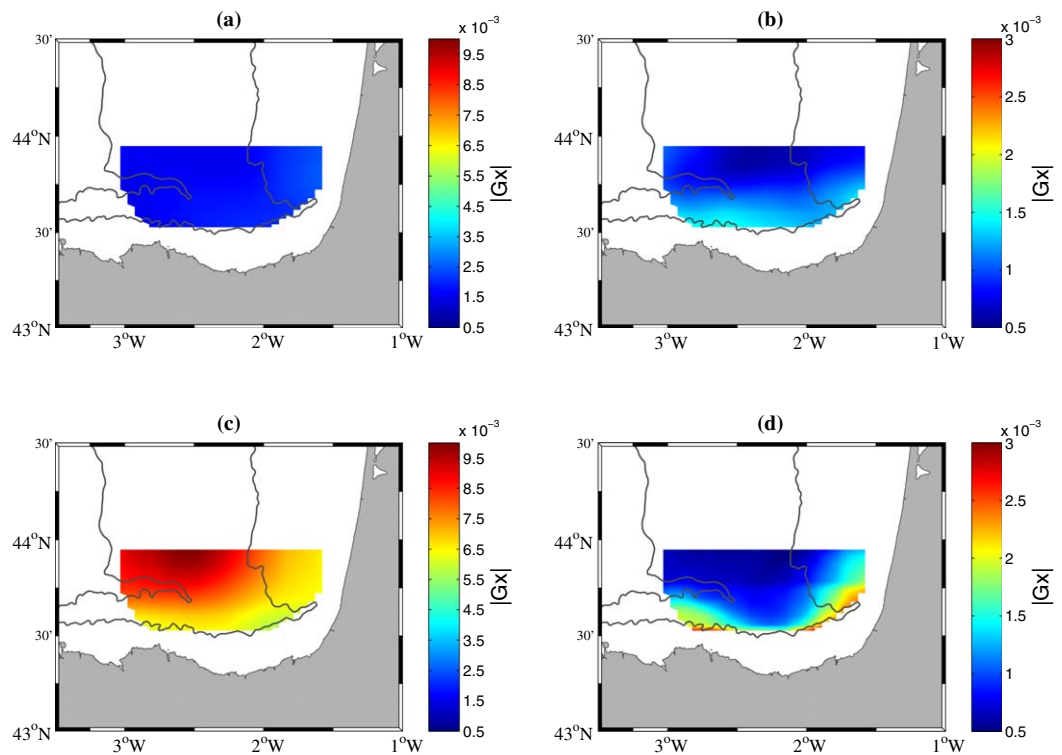
**Figure 6.** Amplitude of the anisotropic transfer functions for the (a and c) zonal and the (b and d) meridional winds at: (a and b) $\omega = -f$ and (c and d) $\omega \approx 0$. Bathymetric contours show the 200 and 2000 m isobaths.

energy of the transfer function at the near-inertial frequency decreases toward the coast (Figures 6a and 6b); this is consistent with the fact that the coastal boundaries inhibit circular motions. This finding is in agreement with the results of *Rubio et al.* [2011]; *Solabarrieta et al.* [2014], who concluded, based on the same HF radar data for the period 2009 and 2009–2011, respectively, that the near-inertial kinetic energy decreases onshore. In contrast, at the low frequencies, the transfer function increases toward the coast (Figures 6c and 6d). This results from the geostrophic balance between the cross-shore pressure gradient and the Coriolis forces such as the surface currents flow parallel to the coast. Recent investigations of *Kim et al.* [2009, 2010] found similar behavior offshore southern California.

## 6. Seasonal Variability of the Anisotropic Transfer Functions

The spatial structure of the anisotropic transfer function at the near-inertial frequency and at the low-frequency in winter and summer is presented in Figure 7. Winter is defined as January, February, and March and summer as July, August, and September [*Fontán et al.*, 2008]. For simplification, only the transfer function for the zonal wind is shown ($\mathbf{G}_x$). Again, the strength of the transfer function at the near-inertial frequency decreases onshore in summer (Figure 7c) due to the effect of the coastline which inhibits circular motions, although the gradient is small in winter (Figure 7a). Conversely, the transfer function at the low-frequency is enhanced onshore (Figures 7b and 7d) as a result of the geostrophic balance, with the effect again stronger in summer. These results are similar to those of the 2 year period in Figure 6, but there are seasonal differences in the strength of the transfer function. The amplitude of the transfer function at both the near-inertial and the low-frequency is stronger in summer (Figures 7c and 7d) than the amplitude in winter (Figures 7a and 7b) and that found considering the full 2 year period record (Figure 6). In summer, the magnitude of the transfer function at the two frequencies is expected to be higher as a result of the presence of shallower mixed layer; conversely, the deeper mixed layer in winter results in a weaker transfer function. In other words, the transference of momentum from a given wind forcing is distributed over a shallower layer in a stratified water column, leading to a stronger surface current response, whereas it is weaker but deeper in well-mixed waters. The estimated transfer functions at the near-inertial frequency show a significant negative linear dependence (correlation coefficients of $-0.7$) with the mixed layer depth

**Figure 7.** Amplitude of the anisotropic transfer functions for the zonal winds at: (a and c) $\omega = -f$ and (b and d) $\omega \approx 0$ (a and b) in winter and (c and d) in summer. Bathymetric contours show the 200 and 2000 m isobaths.

climatology in the study area (not shown). This finding confirms previous results and it is in agreement with studies of, e.g., *Ardhuin et al.* [2009], *Dzwonkowski et al.* [2009], *Kim et al.* [2010, 2015].

## 7. Conclusions

This investigation has estimated the relation between wind and surface current as measured by HF radar at periods shorter than 20 days for the SE Bay of Biscay. The relation is described by the impulse response function in the time domain and the transfer function in the frequency domain, relating HF radar surface currents to NCEP reanalysis surface winds. It is calculated using weighted and tapered linear regression models to build in prior information, such as the expected decay of the response with increasing time lag, and to prevent artificial regression skill. The transfer functions show a strong, sharp peak centered on the clockwise near-inertial frequency, with weaker peaks at low-frequency and centered on the anticlockwise near-inertial frequency. The sharp near-inertial peak corresponds to an exponential decay time scale of about 2.5 days, which is a measure of the energy loss and possibly propagation of the near-inertial waves. The near-inertial response can be seen out to 10 days in the impulse responses (Figures 4c, 4d, 5e, and 5f).

Regressions enforcing isotropy were compared with regressions allowing anisotropy, meaning differing relative responses to different wind directions with the expectation that proximity to the coast would produce anisotropy, as had been seen elsewhere [*Ng*, 1993; *Kim et al.*, 2009]. The results indicate that the response of the ocean to the wind forcing is slightly anisotropic, especially in the SE Bay of Biscay, where the change in the coastline orientation results in a complex water circulation response. Namely, the presence of the coastline causes an anisotropic response of the ocean to the wind forcing. This is observed for both near-inertial motions and low-frequency currents. Spatially, the near-inertial and the low-frequency responses differ from coastal to open ocean. The coastline inhibits circular motions in such a way that the near-inertial currents decrease onshore. In contrast, the parallel low-frequency response is enhanced nearshore as a consequence of the geostrophic balance between the cross-shore pressure gradient and the Coriolis forces.

The spatial structure of the transfer function at the near-inertial frequency and low-frequency also shows seasonal variability. In summer, the response of the ocean current to the wind forcing is larger but shallower in relation to the stratification; in winter, the response is weaker but deeper due to the well-mixed conditions of the water column.

Finally, it is worth noting that the understanding of the coastal response to wind forcing has a broad range of applications concerning the understanding of the ecological response to air-sea coupling and the statistical prediction of surface circulation. The applications include the prediction of the transport of pollutants, biology and oil spills, search and rescue, marine safety, offshore operations, risk assessment, etc. These simple regression models provide a low-cost way to quickly transform wind forecasts into surface current forecast for rapid response. In addition, the observed response functions can be used as a benchmark to test and improve numerical models [e.g., *MacMynowski and Tziperman*, 2010], which is of interest to the community dealing with the prediction of the upper ocean circulation. Furthermore, the statistical current response model could be coupled to ecological models to describe the physical-biological interactions. This, in turn, is also of special interest in fisheries management and assessment in the study area.

# References

Álvarez, I., M. Gómez-Gesteira, M. deCastro, and D. Carvalho (2014), Comparison of different wind products and buoy wind data with seasonality and interannual climate variability in the southern Bay of Biscay (2000–2009), *Deep Sea Res., Part II*, *106*, 38–48, doi:10.1016/j.dsr2.2013.09.028.

Álvarez Salgado, X., J. Herrera, J. Gago, P. Otero, J. Soriano, C. Pola, and C. García-Soto (2006), Influence of the oceanographic conditions during spring 2003 on the transport of the Prestige tanker fuel oil to the Galician coast, *Mar. Pollut. Bull.*, *53*(5–7), 239–249.

Ardhuin, F., L. Marié, N. Rascle, P. Forget, and A. Roland (2009), Observation and estimation of Lagrangian, Stokes and Eulerian currents induced by wind and waves at the sea surface, *J. Phys. Oceanogr.*, *39*(11), 2820–2838.

Dzwonkowski, B., J. Kohut, and X.-H. Yan (2009), Seasonal differences in wind-driven across-shelf forcing and response relationships in the shelf surface layer of the central mid-Atlantic bight, *J. Geophys. Res.*, *114*, C08018, doi:10.1029/2008JC004888.

Ekman, V. (1905), On the influence of the Earth's rotation on ocean-currents, *Ark. Mat. Astron. Fysik*, *2*(11), 1–53.

Elipot, S. (2006), Spectral characterization of Ekman velocities in the Southern Ocean based on surface drifter trajectories, PhD thesis, Scripps Inst. of Oceanogr., San Diego, Calif.

Elipot, S., and S. Gille (2009), Ekman layers in the Southern Ocean: Spectral models and observations, vertical viscosity and boundary layer depth, *Ocean Sci.*, *5*(2), 115–139.

Esnaola, G., J. Sáenz, E. Zorita, A. Fontán, V. Valencia, and P. Lazure (2013), Daily scale wintertime sea surface temperature and IPC-Navidad variability in the southern Bay of Biscay from 1981 to 2010, *Ocean Sci.*, *5*(2), 115–139.

Ferrer, L., A. Fontán, J. Mader, G. Chust, M. González, V. Valencia, A. Uriarte, and M. Collins (2009), Low-salinity plumes in the oceanic region of the Basque Country, *Cont. Shelf Res.*, *29*(8), 970–984, doi:10.1016/j.csr.2008.12.014.

Fontán, A. (2013), Variability in the air-sea interaction spatial patterns and time-scales, within the southeastern Bay of Biscay, PhD thesis, Dep. of Appl. Phys. II, Fac. of Sci. and Technol., Univ. of the Basque Country.

Fontán, A., V. Valencia, A. Borja, and N. Goikoetxea (2008), Oceano-meteorological conditions and coupling in the southeastern Bay of Biscay, for the period 20012005: A comparison with the past two decades, *J. Mar. Syst.*, *72*(14), 167–177, doi:10.1016/j.jmarsys.2007.08.003.

Fontán, A., M. González, N. Wells, M. Collins, J. Mader, L. Ferrer, G. Esnaola, and A. Uriarte (2009), Tidal and wind-induced circulation within the Southeastern limit of the Bay of Biscay: Pasaia Bay, Basque Coast, *Cont. Shelf Res.*, *29*(8), 998–1007.

Fontán, A., J. Sáenz, M. González, A. Rubio, G. Esnaola, J. Mader, P. Liria, C. Hernández, U. Ganzedo, and M. Collins (2013a), Coastal water circulation response to radiational and gravitational tides within the southeastern Bay of Biscay, *J. Mar. Syst.*, *109*(S, SI), S95–S104.

Fontán, A., G. Esnaola, J. Sáenz, and M. González (2013b), Variability in the air-sea interaction patterns and timescales within the southeastern Bay of Biscay, as observed by HF radar data, *Ocean Sci.*, *9*(2), 399–410.

García-Soto, C., R. Pingree, and L. Valdés (2002), Navidad development in the southern Bay of Biscay: Climate change and swoddy structure from remote sensing and in situ measurements, *J. Geophys. Res.*, *107*(C8), 3118, doi:10.1029/2001JC001012.

Gil, J. (2003), Changes in the pattern of water masses resulting from a poleward slope current in the Cantabrian Sea (Bay of Biscay), *Estuarine Coastal Shelf Sci.*, *57*(5–6), 1139–1149.

Gonella, J. (1972), A rotary-component method for analysing meteorological and oceanographic vector time series, *Deep Sea Res. Oceanogr. Abstr.*, *19*(12), 833–846.

González, M., A. Uriarte, A. Fontán, J. Mader, and P. Gyssels (2004), Marine dynamics, in *Oceanography and Marine Environment of the Basque Country, Elsevier Oceanogr. Ser.*, vol. 70, edited by A. Borja and M. Collins, pp. 133–157, Elsevier, Amsterdam, Netherlands.

Herbert, G., N. Ayoub, P. Marsaleix, and F. Lyard (2011), Signature of the coastal circulation variability in altimetric data in the southern Bay of Biscay during winter and fall 2004, *J. Mar. Syst.*, *88*(2), 139–158.

Ibáñez, M. (1979), Hydrological studies and surface currents in the coastal area of the Bay of Biscay, *Lurralde*, *2*, 37–75.

Kim, S., and P. Kosro (2013), Observations of near-inertial surface currents off Oregon: Decorrelation time and length scales, *J. Geophys. Res. Oceans*, *118*, 3723–3736, doi:10.1002/jgrc.20235.

Kim, S., B. Cornuelle, and E. Terrill (2009), Anisotropic response of surface currents to the wind in a coastal region, *J. Phys. Oceanogr.*, *39*(6), 1512–1533.

Kim, S., B. Cornuelle, and E. Terrill (2010), Decomposing observations of high-frequency radar-derived surface currents by their forcing mechanisms: Locally wind-driven surface currents, *J. Geophys. Res.*, *115*, C12007, doi:10.1029/2010JC006223.

Kim, S., G. Gopalakrishnan, and A. Pontel (2015), Interpretation of coastal wind transfer functions with momentum balances derived from idealized numerical model simulations, *Ocean Dyn.*, *65*, 115–141, doi:10.1007/s10236-014-0766-x.

Kim, S. Y., and G. Crawford (2014), Resonant ocean current responses driven by coastal winds near the critical latitude, *Geophys. Res. Lett.*, *41*, 5581–5587, doi:10.1002/2014GL060402.

Koutsikopoulos, C., and B. LeCann (1996), Physical processes and hydrological structures related to the Bay of Biscay anchovy, *Sci. Mar.*, *60*(2), 9–19.

Le Cann, B. (1990), Barotropic tidal dynamics of the Bay of Biscay shelf: Observations, numerical modeling and physical interpretation, *Cont. Shelf Res.*, *10*(8), 723–758.

Le Cann, B., and A. Serpette (2009), Intense warm and saline upper ocean inflow in the southern Bay of Biscay in autumn-winter 2006–2007, *Cont. Shelf Res.*, *29*(8), 1014–1025.

Le Henaff, M., L. Roblou, and J. Bouffard (2011), Characterizing the Navidad current interannual variability using coastal altimetry, *Ocean Dyn.*, *61*(4), 425–437.

MacMynowski, D., and E. Tziperman (2010), Testing and improving ENSO models by process using transfer functions, *Geophys. Res. Lett.*, *37*, L19701, doi:10.1029/2010GL044050.

Ng, B. (1993), The prediction of nearshore wind-induced surface currents from wind velocities measured at nearby land stations, *J. Phys. Oceanogr.*, *23*(8), 1609–1617.

Pingree, R., and B. LeCann (1990), Structure, Strengh and seasonality of the slope currents in the Bay of Biscay region, *J. Mar. Biol. Assoc. U. K.*, *70*(4), 857–885.

Pingree, R., and B. LeCann (1992), 3 anticyclonic Slope Water Oceanic eDDIES (SWODDIES) in the southern Bay of Biscay in 1990, *Deep Sea Res., Part A*, *39*(7–8), 1147–1175.

Río, M., and F. Hernández (2003), High-frequency response of wind-driven currents measured by drifting buoys and altimetry over the world ocean, *J. Geophys. Res.*, *108*(C8), 3283, doi:10.1029/2002JC001655.

Rubio, A., G. Reverdin, A. Fontán, M. González, and J. Mader (2011), Mapping near-inertial variability in the SE Bay of Biscay from HF radar data and two offshore moored buoys, *Geophys. Res. Lett.*, *38*, L19607, doi:10.1029/2011GL048783.

Saha, S., et al. (2010), The NCEP climate forecast system reanalysis, *Bull. Am. Metorol. Soc.*, *91*(8), 1015–1057.

Saha, S., et al. (2014), The NCEP climate forecast system version 2, *J. Clim.*, *27*(6), 2185–2208, doi:10.1175/jcli-d-12-00823.1.

Schmidt, R. (1986), Multiple emitter location and signal parameter estimation, *IEEE Trans. Antennas Propag.*, *34*(3), 276–280.

Simons, T. (1984), Topographic response of nearshore currents to wind: An empirical model, *J. Phys. Oceanogr.*, *14*(8), 1393–1398.

Solabarrieta, L., A. Rubio, S. Castanedo, R. Medina, G. Charria, and C. Hernández (2014), Surface water circulation patterns in the southeastern Bay of Biscay: New evidences from HF radar data, *Cont. Shelf Res.*, *74*, 60–76.

Usabiaga, J. I., J. S. Aguirre, V. Valencia, and Á. Borja (2004), Climate and meteorology: Variability and its influence on the ocean, in *Oceanography and Marine Environment of the Basque Country, Elsevier Oceanogr. Ser.*, vol. 70, edited by Á. Borja and M. Collins, chap. 4, pp. 75–95, Elsevier, Amsterdam, Netherlands, doi:10.1016/S0422-9894(04)80042-4.

Weller, R. (1981), Observations of the velocity response to wind forcing in the upper ocean, *J. Geophys. Res.*, *86*, 1969–1977, doi:10.1029/JC086iC03p01969.

Wunsch, C. (1996), *The Ocean Circulation Inverse Problem*, 442 pp., Cambridge Univ. Press, Cambridge, U. K.

Yoshikawa, Y., and A. Masuda (2009), Seasonal variations in the speed factor and deflection angle of the wind-driven surface flow in the Tsushima Strait, *J. Geophys. Re.*, *114*, C12022, doi:10.1029/2009JC005632.